Uthman, M., Rahman, B. M., Kejalakshmy, N., Agrawal, A. & Grattan, K. T. V. (2012). Design and Characterization of Low-Loss Porous-Core Photonic Crystal Fiber. IEEE Photonics Journal, 4(6), pp. 2315-2325. doi: 10.1109/JPHOT.2012.2231939

IEEE Photonics Journal
An IEEE Photonics Society Publication

Open Access

Design and Characterization of Low-Loss Porous-Core Photonic Crystal Fiber

Volume 4, Number 6, December 2012

M. Uthman
B. M. A. Rahman
N. Kejalakshmy
A. Agrawal
K. T. V. Grattan

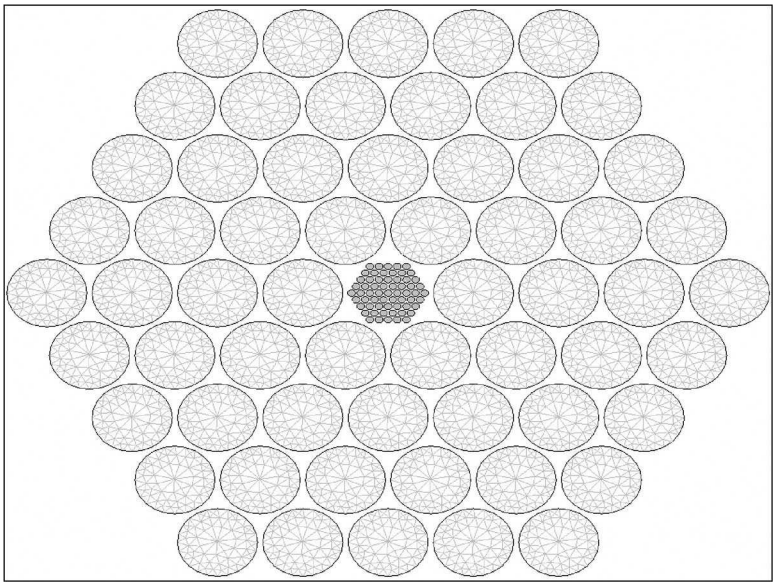

DOI: 10.1109/JPHOT.2012.2231939
1943-0655/$31.00 ©2012 IEEE

IEEE photonics SOCIETY

IEEE

Design and Characterization of Low-Loss Porous-Core Photonic Crystal Fiber

M. Uthman, B. M. A. Rahman, N. Kejalakshmy, A. Agrawal, and K. T. V. Grattan

School of Engineering and Mathematical Sciences, City University, EC1V 0HB London, U.K.

DOI: 10.1109/JPHOT.2012.2231939
1943-0655/$31.00 ©2012 IEEE

Manuscript received November 9, 2012; revised November 30, 2012; accepted November 30, 2012. Date of publication December 5, 2012; date of current version December 14, 2012. Corresponding author: M. Uthman (e-mail: m.uthman@yahoo.com).

Abstract: A rigorous modal solution approach, based on the numerically efficient finite-element method (FEM), has been used to design and characterize a photonic crystal fiber (PCF) with a porous air core, which has the potential for use for low-loss guidance of terahertz (THz) waves. Here, for the first time, it is reported that a large fraction of the power that is also well confined in the waveguide can be guided in the low-loss air holes, thus to reduce the overall modal loss. This novel PCF design can readily be fabricated by use of a range of techniques including stack-and-draw, extrusion, and drilling.

Index Terms: Lasers and optoelectronics, optical design, PCF, THz.

1. Introduction

Terahertz radiation (or THz waves), generally identified as covering the 0.1- to 10-THz frequency band, has attracted widespread attention in recent years. Numerous applications of such radiation have been reported including medical diagnostics [1], [2], testing of pharmaceutical drugs [3], and defect detection in electronic circuits [4], among others. Devices operating in the THz regime can be used in hazardous or security sensitive areas for monitoring drugs [5], [6], gas [7], explosives [8], [9], or weapons and also in the study and better understanding of the dynamics of complex natural biological systems. This has led to a concerted effort in the development of better THz sources and detectors and as a result, the last decade has seen significant technical advances in THz wave generation [10] and detection [11], [12]. However, most of the THz systems that are available and for which market introduction are sought are based on free-space transmission, due to the lack of suitable low-loss flexible waveguides.

The development of low-loss THz waveguides has been challenging as almost all presently available materials are highly absorbent in this frequency band. Previously, circular metallic guides, like stainless solid wires [13] or hypodermic needles [14], have been considered, but these waveguide are highly lossy, these being in the order of 500 dB/m. Plasmonic modes are always very lossy, and in case of a metal rod, the mode field also extends well into the outer open space, which is less controllable. Although a THz wave cannot be guided inside a hollow dielectric tube (unless the Bragg principle is used), however, if this tube is coated with a metal layer, a plasmonic mode can form inside the hollow core, where the guiding environment can be better controlled or manipulated. It has been shown that, by incorporating an additional thin dielectric layer [15], the mode field can be drawn away from the lossy plasmonic interface and, as a consequence, the overall loss value can be reduced [16]. However, often, these waveguides have rather large diameter and not very flexible, and for a small diameter, the loss value also increases.

On the other hand, most of the optical waveguides are dielectric waveguides, which arises due to the availability of very low-loss materials at these important wavelengths. Previously, it had been demonstrated that a simple polyethylene (PE) fishing line can guide THz waves [17]. Currently, polymers are the materials of choice for making flexible THz dielectric waveguides, i.e., polymethyl methacrylate (PMMA) [18], Teflon [19], high-density PE (HDPE) [17], [20], and Topas [21] are widely used as they have the lowest reported losses in the THz frequency range and they are relatively easy to process. Jin *et al.* [22] have carried out an extensive study on the loss values of various polymer materials in the THz frequency range.

However, because the absorption losses in these dielectric materials are still very high, a variety of guiding mechanism have been reported to reduce the overall modal losses. Dry air has one of lowest material losses in the THz frequency range. When a dielectric rod is surrounded by air, operating very close to its cutoff condition leads the mode field to extend into the low index air cladding region, and such subwavelength waveguides have been reported [17]. The main disadvantage of this design is that mode extends considerably into the surrounding air cladding and the power is propagated mostly outside the waveguide: this strongly interacts with the surrounding environment, and the bending loss would also be expected to be excessively high.

It has also been reported that polystyrene foam [23], with its large air fraction ratio, can have lower overall material loss, but with its refractive index close to 1.02, it needs not only air cladding for total internal reflection (TIR) based guidance but also a larger dimension to confine most of the THz waves in its core: this is difficult for many practical applications.

Following the principle of Bragg guidance in optical fiber, hollow core designs have also been considered for guiding THz waves [24], [25]. Neilsen *et al.* [26] have also reported a microstructured core and honeycomb band-gap THz fiber. However, it is well known that these are narrow-band waveguides and strict periodicity needs to be maintained to satisfy the Bragg conditions.

Recently, it has been shown that, in silicon slot waveguides [27], [28], light can be guided in the low index air region. Using this concept, Nagel *et al.* [29] have reported the use of subwavelength air hole within a solid silica core to increase the power fraction within the air hole to reduce the loss. Similarly, Kejalakshmy *et al.* [30] have reported on a Teflon photonic crystal fiber (PCF) with metal-clad hollow defect-core supporting plasmon modes for possible THz sensing applications.

PCF is a class of optical fiber where many air holes run along the length of the waveguide [31] and where light is guided by the modified TIR when the equivalent refractive index of the porous cladding is less than that of the solid core. PCFs are being used as waveguides, which exploit their unique characteristics of being endlessly single moded and which offer adjustable spot-size and dispersion properties for various linear and nonlinear applications. As a fraction of the power can be confined and guided in the air holes, recently, Han *et al.* [20] and Goto *et al.* [19] have fabricated HDPE and Teflon PCF, respectively. However, in both cases, the core being a solid dielectric has not made it possible to reduce the modal loss significantly.

Recently, Hassani *et al.* [32] and Ung *et al.* [33] have reported a porous-core design to take advantage of the guiding offered through the low-loss air holes. In this case, they have used a relatively larger d/Λ ratio (of 0.95) to have a larger power fraction in the air holes (where d is the air-hole diameter and the pitch Λ is the center-to-center distance between two adjacent air holes). However, as a large d/Λ is used in this case, the equivalent index of the core was very low, and the authors had to consider air cladding for the TIR. As a consequence, they also had to consider a large core diameter, which was 70 times the operating wavelength, equal to 21 mm for mode confinement as the index contrast between the porous core and air cladding was very small. In their work [32], they report the maximum confinement in the air holes of the core was around 58%, and in that design, the total power in the air was around 80%, which indicates that remaining 20% power was confined in the solid PE. They have also mentioned that total confinement in the PE could be as low as 8%, and in that case, the expected loss value would be only 10 dB/m.

In this paper, a novel concept, using porous core and *also* porous cladding, is reported. In this case, the d/Λ ratio of the cladding air holes must be larger than that in the core to create a differential index contrast to confine the THz waves within the waveguide. In this case, all the power will be fully confined inside the waveguide, and the system performance will not be affected by the

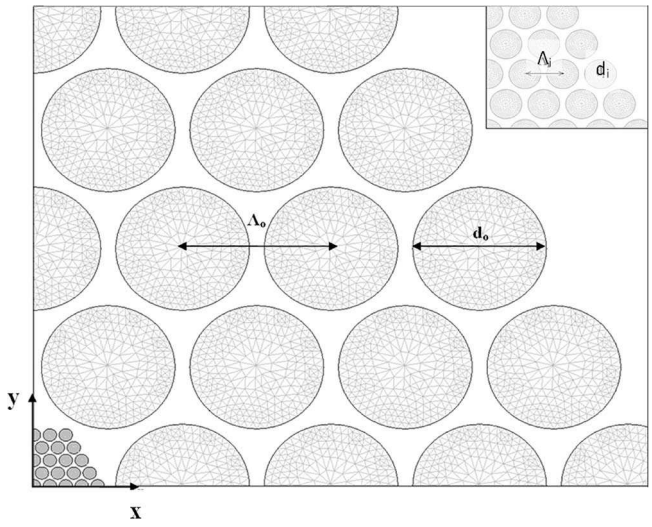

Fig. 1. Representation of the porous-core PCF cross-section with $N_{core} = 4$, $N_{clad} = 4$. Λ_o = outer pitch and d_o = outer radius. Inset shows Λ_i = inner pitch and d_i = inner radius.

surrounding medium. Here, optimization of the power fraction in the air holes is shown, with the fabrication parameters, including their bending loss calculations.

2. Numerical Solution

In the modal solution approach based on the finite-element method (FEM), the intricate cross section of a PCF and its microstructured core can be represented by using many triangles of different shapes and sizes. This flexibility makes the FEM preferable as a technique to use when compared with the finite-difference method, which not only uses inefficient regular-spaced meshing but also cannot represent slanted or curved dielectric interfaces. The optical modes in a high index contrast PCF with 2-D confinement are also hybrid in nature, with all six components of the **E** and **H** fields being present. It is also known that the modal hybridness is enhanced by the presence of slanted or curved dielectric interfaces. Hence, not only is a vectorial formulation needed for the accurate determination of their modal solutions, but also, a proper representation of the dielectric interfaces is important. In the present approach, an **H**-field-based rigorous full-vectorial FEM has been used to analyze the operation of PCFs with air holes arranged in a triangular lattice in the Teflon cladding. The **H**-field formulation developed previously [34] is a valid approach for microwave and optical guided-wave devices, including the intermediate THz frequency range. This **H**-field formulation with the augmented penalty function technique is given as

$$\omega^2 = \frac{\left(\int (\nabla \times \vec{H}) * \cdot \hat{\varepsilon}^{-1} (\nabla \times \vec{H})\, d\Omega\right) + \left(\int (\alpha/\varepsilon_o)(\nabla \cdot \vec{H}) * (\nabla \cdot \vec{H})\, d\Omega\right)}{\int \vec{H} * \cdot \hat{\mu} \vec{H}\, d\Omega} \tag{1}$$

where $\vec{H}$ is the full-vectorial complex magnetic field; $\hat{\varepsilon}$ and $\hat{\mu}$ are the permittivity and permeability, respectively, of the waveguide; ε_o is the permittivity of the free space; ω^2 is the eigenvalue (where ω is the angular frequency of the wave); and α is a dimensionless parameter used to impose the divergence-free condition of the magnetic field in a least-square sense. In this formulation, both the $\hat{\varepsilon}$ and $\hat{\mu}$ parameters can be arbitrary complex tensors with possible off-diagonal coefficients, suitable to characterize electro-optic, acousto-optic, and elasto-optic devices. When necessary, to calculate the leakage and bending losses, perfectly matched layers (PMLs) [35] have been incorporated around the computation window, but this also transforms the resulting formulation to a complex eigenvalue equation.

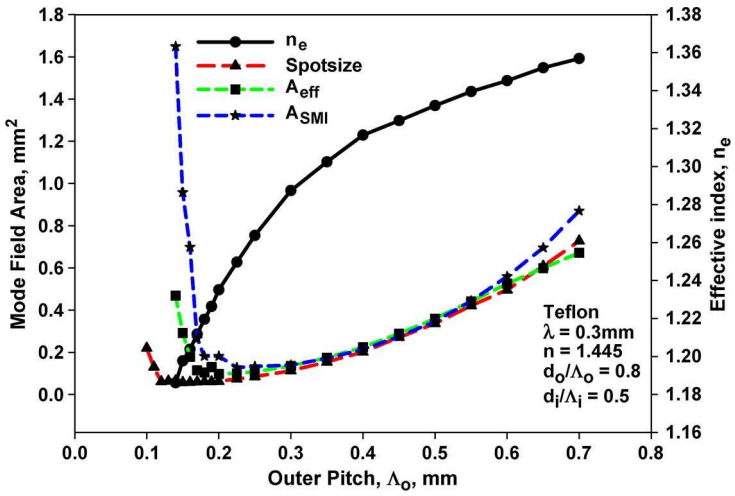

Fig. 2. Variations of the mode field areas and effective index with the pitch, Λ_o for $d_o/\Lambda_o = 0.8$ and $d_i/\Lambda_i = 0.5$.

3. Results

In this paper, a Teflon PCF is considered with the number of air-hole rings, $N_{clad} = 4$ in the cladding and also $N_{core} = 4$ in the core. To achieve the maximum porosity, at the center of the core, a similar air hole is considered rather than a solid rod. In this case, if the outer pitch Λ_o is equal to diameter of the porous core (D), which is nine times $(2 * N_{core} + 1)$ the inner pitch Λ_i, then it would be easier to use the conventional stack-and-draw technique to fabricate such a porous-core PCF. The refractive index of Teflon is taken to be 1.445. In this case, the bulk material loss for Teflon has been considered to be 0.3 cm^{-1} or 130 dB/m [32], at 1 THz. This gives the imaginary part of the refractive index as 0.000715 at the operating frequency of 1 THz $(\lambda = 0.3$ mm$)$, which is used in this work. The overall structure has a two-fold symmetry, so only a quarter of the PCF is simulated as shown in Fig. 1. In total, 80 000 first-order triangular elements of different sizes are used to represent a quarter of the structure. The porous core is also shown as an inset at the top right corner of this figure.

It has been mentioned that the inner air-hole diameter/pitch ratio (d_i/Λ_i) in the core needs to be smaller than that of the cladding (d_o/Λ_o) to have a higher equivalent index necessary to support the TIR guidance. In this case, initially, (d_i/Λ_i) is taken as 0.5, and $(d_o/\Lambda_o) = 0.8$. Variations of the effective index and the mode-size areas with the outer pitch Λ_o are shown in Fig. 2. It can be observed that, as the pitch value is reduced, the effective index of the fundamental H_{11}^x mode is also reduced. The cutoff condition is reached when the effective index approaches the equivalent index, often designated as N_{fsm} [36] of the cladding. Here, the effective index N_e is defined as $N_e = \beta/k_o$, where β is the propagation constant of the mode and k_o is the wavenumber. For this structure, the 90° rotational symmetry is nearly satisfied, so the modal properties of the quasi-TE (H_{11}^y) and quasi-TM (H_{11}^x) modes would be almost identical.

Variations of the mode-size areas with the pitch are also shown in Fig. 2. There have been different definitions used to quantify this mode-size area, and for a Gaussian-shaped field profile, they give identical results [37]. The spot size, given as σ, can be defined as the area where the power density is higher than $1/e^2$ of the maximum power density. On the other hand, the effective area A_{eff} can be defined as $((\int |E|^2)dA)^2/(\int |E|^4 dA))$, where E is the electric-field profile. The area second moment of the optical intensity $A_{SMI} = 2\sqrt{((\int x^2 I(x,y)/(\int I(x,y)))}$, where $I(x,y)$ is the second moment of intensity distribution profile.

It can be observed that, as the outer pitch d_o/Λ_o is reduced, initially, the mode-size areas reduce since the core size is also being reduced. All three mode area definitions give similar values when $\Lambda_o = 0.45$ mm, as in this case, the field profile is close to a Gaussian shape. However, when the

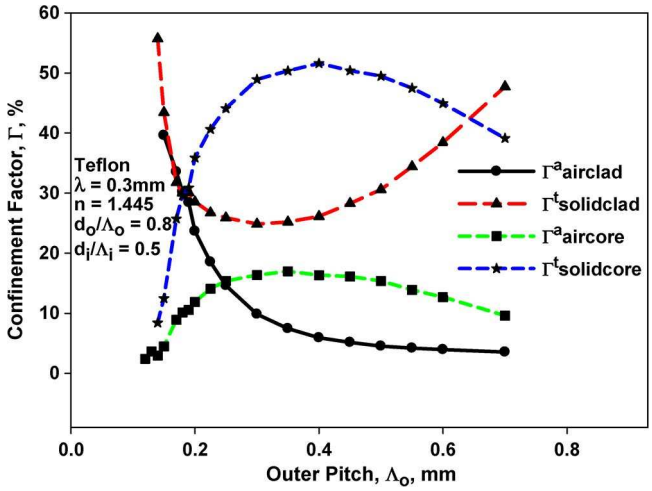

Fig. 3. Variation of the confinement factors with the outer pitch, Λ_o, for $d_o/\Lambda_o = 0.8$ and $d_i/\Lambda_i = 0.5$.

pitch is reduced further, the mode-size areas start to increase as the mode approaches its cutoff condition. In this case, a greater amount of the modal field will extend into the cladding areas. It should be noted that, when Λ_o is reduced, the inner pitch Λ_i is also reduced to maintain their constant ratio to be 9, necessary for this design with $N_{\text{core}} = 4$.

The variations of the power confinement in various regions with the outer pitch Λ_o are shown in Fig. 3. The power confinement factor Γ was determined for different regions of the porous-core PCF, normalized to the total power. The confinement factor can be calculated by integrating the Poynting vector over a given region Ω_i as

$$\Gamma_i = \int_{\Omega i} \{\mathbf{E}^* \times \mathbf{H}\} \mathbf{d}\Omega \tag{2}$$

where **E** is the electric field, and **H** is the magnetic field of the mode. In this full-vectorial approach, all the six components of the **E** and **H** fields are used for the calculation of the confinement factors. Four regions have been clearly identified, air holes in core, Teflon in core, air holes in cladding, and Teflon in cladding as $\Gamma^a_{\text{aircore}}$, $\Gamma^t_{\text{solidcore}}$, $\Gamma^a_{\text{airclad}}$, and $\Gamma^t_{\text{solidclad}}$, respectively.

It can be observed that as the pitch Λ_o is reduced, the power in the Teflon-core region $\Gamma^t_{\text{solidcore}}$, shown by stars, initially increased and then subsequently reduced as the mode approaches its cutoff, when most of the power extends into the cladding. Similar feature are shown for the power in the air holes of the core region $\Gamma^a_{\text{aircore}}$, represented by squares. On the other hand, the power in the solid Teflon area of the clad $\Gamma^t_{\text{solidclad}}$, shown by triangles, initially reduces with the pitch Λ and then increases when the mode approaches its cutoff condition and the power extends further into the cladding. However, the power in the cladding air holes $\Gamma^a_{\text{airclad}}$, shown by circles, monotonically increases as the pitch Λ_o is reduced and increases more rapidly when the cutoff condition approaches. It can be observed that the maximum confinement in the Teflon core $\Gamma^t_{\text{solidcore}}$ is about 52%, whereas the confinement in the air holes in core $\Gamma^a_{\text{aircore}}$ is only 17%, when the outer pitch $\Lambda_o = 0.35$ mm. To understand the complex interaction between these parameters, next, the field profiles for two pitch values are shown.

The variations of the H_x fields of the fundamental H^x_{11} mode along the horizontal axis are shown in Fig. 4 for two different pitch values. For a higher pitch value $\Lambda_o = 0.7$ mm, the field profile shown in Fig. 4(a) demonstrate a reasonably well-confined mode inside the core with its decay length ($1/e$ of the maximum field) as 0.12 mm. The field variation inside the core clearly shows the presence of the five air holes (shown by arrows), along the *x*-axis with their local field minima. In this case, near the outer air-hole ring (of the inner core), the modal field shows its maximum value due to the presence of a large solid Teflon areas just before the first air-hole ring in the cladding. In this case,

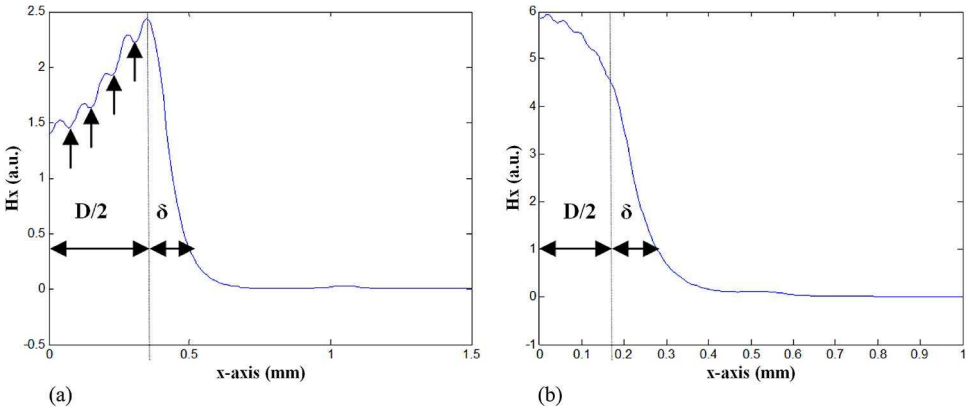

Fig. 4. Variations of the H_x field of the H_{11}^x mode along the x-axis for (a) $\Lambda_o = 0.7$ mm and (b) $\Lambda_o = 0.35$ mm, when $d_o/\Lambda_o = 0.8$, and $d_i/\Lambda_i = 0.50$.

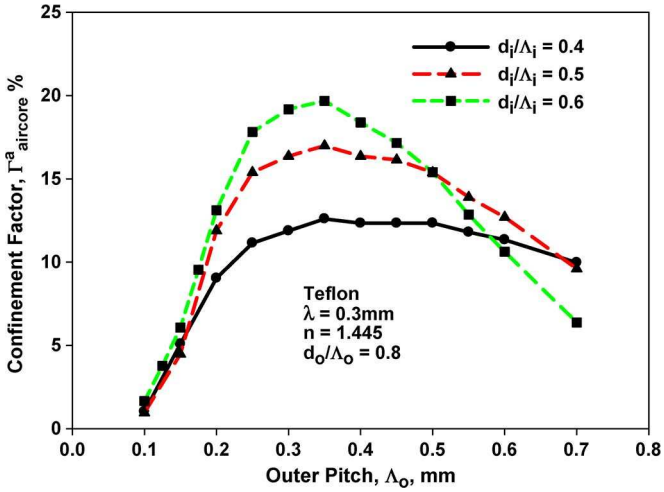

Fig. 5. Variation of the confinement factor in the core air holes, $\Gamma^a_{\text{aircore}}$, with the outer pitch Λ_o for $d_o/\Lambda_o = 0.8$ but with different d_i/Λ_i values.

total confinement in the core was around 50%. On the other hand, for a smaller outer-pitch value $\Lambda_o = 0.35$ mm, as shown in Fig. 4(b), field is more confined in the core $(\Gamma_{\text{core}} = 52\%)$ but associated with a slower decay (decay length 0.18 mm) in the cladding.

The variations of the power confinements in the core air holes with the outer pitch Λ_o are shown in Fig. 5. It can be observed that, as the outer pitch Λ_o is reduced, the power confinement in the core air holes $\Gamma^a_{\text{aircore}}$ increases and reaches a maximum value. A further reduction of the pitch value brings this mode closer to cutoff, and the mode field extends in the outer cladding so $\Gamma^a_{\text{aircore}}$ reduces. It is also shown that, as the d_i/Λ_i increases from 0.4 to 0.6, the maximum confinement in the core air holes $\Gamma^a_{\text{aircore}}$ also increases. This maximum value is identified as $\Gamma^{\text{max}}_{\text{air-core}}$. It can be observed here that, in all the three cases, the maximum power in the core was obtained when the outer pitch Λ_o was around 0.35 mm. However, there is a limit to the increment of the value of d_i/Λ_i, as this needs to be lower than the outer d_o/Λ_o value to have sufficient index contrast for the TIR guidance. To increase the air-filling area and also to avoid the field localization at the core–cladding interface, it was considered to increase both the d_i/Λ_i and d_o/Λ_o values to reduce the solid Teflon area near the core–cladding boundary.

Further, besides varying the Λ_o and the inner d_i/Λ_i values, the outer d_o/Λ_o values are also adjusted to get the maximum confinement in the core air holes $\Gamma^{\text{max}}_{\text{air-core}}$. The variations of the

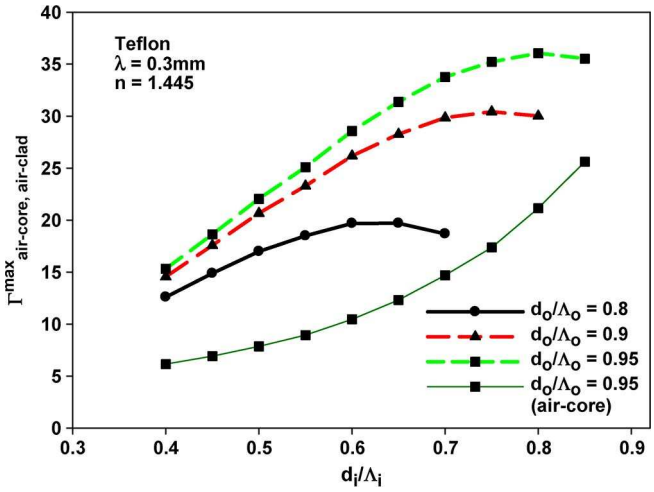

Fig. 6. Variation of the maximum confinement factor in the air holes with the d_i/Λ_i for some fixed d_o/Λ_o values.

maximum power confinement in the core air holes with the inner d_i/Λ_i are shown in Fig. 6. For given values of d_o/Λ_o and d_i/Λ_i, the pitch Λ_o is adjusted to achieve the maximum power confinement in the core air holes $\Gamma^{max}_{air\text{-}core}$. The variation of this value with d_i/Λ_i is shown for a fixed d_o/Λ_o. It was noted that, for most of the cases, the outer pitch Λ_o was around 0.35 mm to achieve the maximum confinement in the core air holes. It can be observed that, as the value of d_i/Λ_i is increased, the maximum power confinement in the core air holes also increases. However, a further increase in d_i/Λ_i reduces the index contrast between the core and cladding, and $\Gamma^{max}_{air\text{-}core}$ reduces as more power is extended in the cladding. It can also be noted that $\Gamma^{max}_{air\text{-}core}$ increases as the d_o/Λ_o is increased. The confinement in the cladding air holes is also shown by a solid-green line with rectangles but only for $d_o/\Lambda_o = 0.95$ and $\Lambda_o = 0.35$ mm. It can be observed that total power in the air holes (both in core and cladding) reaches 58%, when $d_o/\Lambda_o = 0.95$ and $d_i/\Lambda_i = 0.85$. By increasing the ratio d_o/Λ_o, the maximum confinement in the air holes Γ_{max} also increases, but this also needs a higher value of d_i/Λ_i. It is noted here that reducing the difference between the outer/inner d/Λ ratios increases the maximum power confinement in the core air holes. If it is possible to increase d_i/Λ_i to more than 0.85 (and d_o/Λ_o more than 0.95), the power fraction in the air holes can be increased further. In the design reported [32], d_i/Λ_i has been considered as 0.95, and as a consequence, it had been necessary to consider an air cladding (porous cladding with air holes is not possible) to achieve the index contrast necessary for the TIR guidance and thus exposing the mode to external environmental influences.

It was observed that, for all the d/Λ used in this paper, for both inner and outer air holes, as the Λ is reduced, the mode areas reach a minimum value and then expands as the modal cutoff approaches. However, for a given d_o/Λ_o, when d_i/Λ_i is reduced, although the features remain similar, minimum mode area value is reduced and the mode cutoff condition arrives at a slightly lower Λ value. In all the cases, when power in the air holes are maximized, the PCF has been single moded.

Fig. 7 shows the H_x field variation along the x-axis for the fundamental H^x_{11} mode when $\Lambda_o = 0.35$ mm, $d_o/\Lambda_o = 0.95$, and $d_i/\Lambda_i = 0.85$, a combination which achieved the maximum power confinement in the air holes. Here, the field profile is almost constant within the core with small ripples due to the presence of the air holes inside the core. In this case, the index contrast between core and cladding is smaller, and the field extends in the cladding region with the $1/e$ decay length given by 0.23 mm but most of the power is well confined inside the waveguide. One local field maximum is shown by an arrow identifying the location between the first and second air-hole rings where the field value is about 0.004% of the maximum field. This also signifies that the THz energy is well confined inside the cladding and does not extend outside the waveguide, unlike

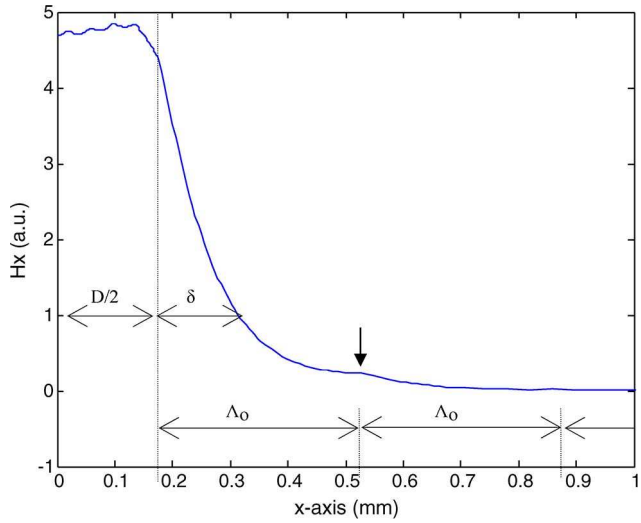

Fig. 7. Variation of the H_x field along the x-axis for the H_{11}^x mode when $\Lambda_o = 0.35$ mm, $d_o/\Lambda_o = 0.95$ and $d_i/\Lambda_i = 0.85$.

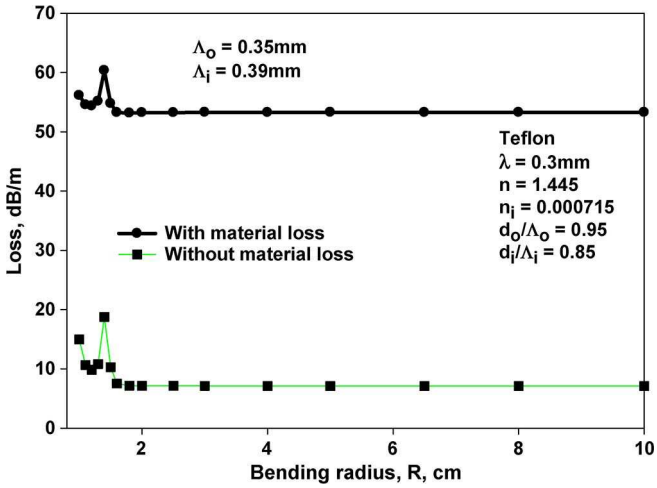

Fig. 8. Variation of bending loss with bending radius, R at $\Lambda_o = 0.35$ mm and $\Lambda_i = 0.039$ mm.

the waveguides with air cladding [32], when the field extends in the air cladding and the mode would be influenced by both environmental factors and bending.

Modal loss and the bending loss of this porous-core PCF have also been studied. In this analysis, a Conformal Transformation [38], [39] was carried out to obtain the equivalent index of a bent PCF, and PML regions [35], [40] are introduced to absorb the leaking power. For a bent PCF, only onefold symmetry is available, and symmetry along the vertical axis is destroyed. Fig. 8 shows the variation of the loss values for a bent PCF with the bending radius R. In this case, for the porous-core PCF, the parameters are taken to be $\Lambda_o = 0.35$ mm, $d_o/\Lambda_o = 0.95$, and $d_i/\Lambda_i = 0.85$. Initially, the material loss is ignored, and the bending and leakage loss is shown by a dashed curve with solid squares. When bending radius is large, the loss value is around 8 dB/m, which identifies the leakage loss only. If necessary, this leakage loss can be further reduced by increasing the number of rings in the cladding region (in the present simulation, $N_{clad} = 4$ is considered) or by increasing the d/Λ value of the outer rings. When the bending radius R is reduced, the loss value increases, which now includes the bending loss. It can be noted that, for this particular design, the bending loss

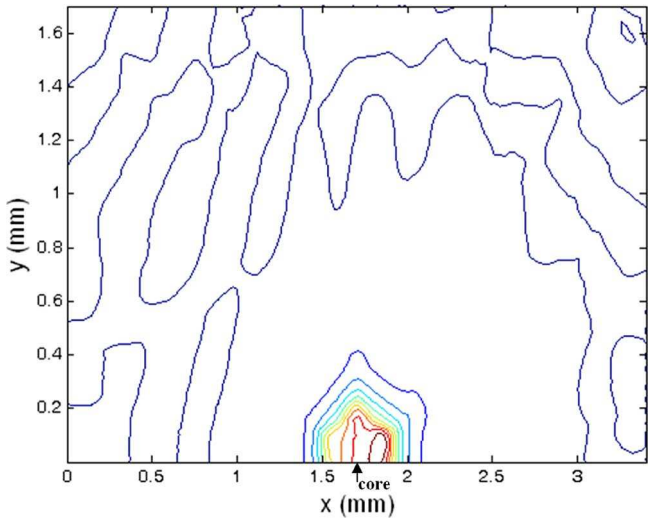

Fig. 9. H_x field profile of the bent PCF for the fundamental H_{11}^x mode for bending radius, 1.5 cm.

is negligible when the bending radius R is above 2 cm. However, as the material loss is the dominant loss-contributing factor, when this is added by considering the imaginary part of the complex refractive index of Teflon, the total loss is shown by a solid line with solid circles. It can be identified that the material loss dominates with its value around 53 dB/m. However, this value is considerably less than that of a solid-core Teflon PCF, which could be as high as the bulk material loss, this being 130 dB/m. It can be noted that the loss value peaks when $R = 1.4$ cm and this is due to the mode coupling between the PCF mode and a cladding mode, and appearance of such more degeneration was reported earlier [40].

The H_x field profile of the bent PCF for the fundamental H_{11}^x mode is shown in Fig. 9, when the bending radius is 1.5 cm. Only half of the PCF structure is shown, as symmetry along the horizontal axis was exploited during the simulation. It can be observed that the center of the mode field has shifted towards the right (away from the bending center) and the influence of the air holes in the first cladding ring is clearly visible.

4. Conclusion

A novel design incorporating both a porous core and *also* a porous clad has been presented here, this being a better design than a PCF with porous cladding [19], [20] or a porous-core [32], [33] fiber with air cladding. In this paper, a rigorous full-vectorial modal solution approach has been used to optimize the index contrast and the dimensions to maximize the power confinement in the air holes.

It has been shown here that, by using a porous core along with the porous cladding of a conventional PCF, the power confinement in the air holes can be significantly increased, which will reduce the effect of material loss by 60% for the solid Teflon. The overall loss value can be further reduced if the material loss can be reduced or the fabrication technology improved to allow a higher d/Λ value than 0.95 (for the outer d/Λ), which is considered in this paper. It has been shown that the leakage loss and the bending losses for such a PCF are very small for practical applications.

The manufacturing technology for PCF operating at optical frequencies has matured, and PCFs with a submicron pitch are routinely being fabricated. Compared with that, PCF for THz frequencies with a pitch 100 times larger would be relatively easy to fabricate, and such a PCF has also been fabricated [19], [20]. In the design reported here, when a THz PCF with additionally porous core [33] is considered, the 20- to 40-μm inner pitch dimensions are easily feasible, and the fabrication process does not introduce any additional challenge. The design shown here, with a fixed Λ_o/Λ_i ratio depending on number of air-hole rings N_{core} in the core, would be compatible for more widely used draw-and-stack approaches.

The availability of a low-loss flexible waveguide will allow both distributing THz waves and also a waveguide to act as part of a functional device for processing the signals. The reliability and the performance of a THz system can be improved by having a compact, flexible, robust, and integrable waveguide for the remote delivery of high power.

References

[1] R. M. Woodward, V. P. Wallace, D. D. Arnone, E. H. Linfield, and M. Pepper, "Terahertz pulsed imaging of skin cancer in the time and frequency domain," *J. Biol. Phys.*, vol. 29, no. 2/3, pp. 257–261, Jan. 2003.

[2] D. A. Crawley, C. Longbottom, B. E. Cole, C. M. Ciesla, D. Arnone, V. P. Wallace, and M. Pepper, "Terahertz pulse imaging: A pilot study of potential applications in dentistry," *Caries Res.*, vol. 37, no. 5, pp. 352–359, Sep./Oct. 2003.

[3] C. J. Strachan, P. F. Taday, D. A. Newnham, K. C. Gordon, J. A. Zeitler, M. Pepper, and T. Rades, "Using terahertz pulsed spectroscopy to quantify pharmaceutical polymorphism and crystallinity," *J Pharm. Sci.*, vol. 94, no. 4, pp. 837–846, Apr. 2005.

[4] T. Kiwa, M. Tonouchi, M. Yamashita, and K. Kawase, "Laser terahertz-emission microscope for inspecting electrical faults in integrated circuits," *Opt. Lett.*, vol. 28, no. 21, pp. 2058–2060, Nov. 2003.

[5] P. U. Jepsen, D. G. Cooke, and M. Koch, "Terahertz spectroscopy and imaging—Modern techniques and applications," *Laser Photon. Rev.*, vol. 5, no. 1, pp. 124–166, Jan. 2011.

[6] K. Kawase, Y. Ogawa, Y. Watanabe, and H. Inoue, "Non-destructive terahertz imaging of illicit drugs using spectral fingerprints," *Opt. Exp.*, vol. 11, no. 20, pp. 2549–2554, Oct. 2003.

[7] R. H. Jacobsen, D. M. Mittleman, and M. C. Nuss, "Chemical recognition of gases and gas mixtures with terahertz waves," *Opt. Lett.*, vol. 21, no. 24, pp. 2011–2013, Dec. 1996.

[8] Y. C. Shen, T. Lo, P. F. Taday, B. E. Cole, W. R. Tribe, and M. C. Kemp, "Detection and identification of explosives using terahertz pulsed spectroscopic imaging," *Appl. Phys. Lett.*, vol. 86, no. 24, pp. 241116-1–241116-3, Jun. 2005.

[9] H. B. Liu, Y. Chen, G. J. Bastiaans, and X. C. Zhang, "Detection and identification of explosive RDX by THz diffuse reflection spectroscopy," *Opt. Exp.*, vol. 14, no. 1, pp. 415–423, Jan. 2006.

[10] R. Kohler, A. Tredicucci, F. Beltram, H. E. Beere, E. H. Linfield, A. G. Davies, D. A. Richie, R. C. Iotti, and F. Rossi, "Terahertz semiconductor-heterostructure laser," *Nature*, vol. 417, no. 6885, pp. 156–159, May 2002.

[11] N. E. Karpowicz, J. Chen, T. Tongue, and X. C. Zhang, "Coherent millimetre wave to mid-infrared measurements with continuous bandwidth reaching 40 THz," *Electron. Lett.*, vol. 44, no. 8, pp. 544–545, Apr. 2008.

[12] Q. Wu, M. Litz, and X. C. Zhang, "Broadband detection capability of ZnTe electro-optic field detectors," *Appl. Phys. Lett.*, vol. 68, no. 21, pp. 2924–2926, May 1996.

[13] K. Wang and D. M. Mittleman, "Metal wires for terahertz wave guiding," *Nature*, no. 7015, pp. 376–379, 432, Nov. 2004.

[14] G. Gallot, S. P. Jamison, R. W. McGowan, and D. Grischkowsky, "Terahertz waveguides," *J. Opt. Soc. Amer. B, Opt. Phys.*, vol. 17, no. 5, pp. 851–863, May 2000.

[15] B. Bowden, J. A. Harrington, and O. Mitrofanov, "Silver/polystyrene-coated hollow glass waveguides for the transmission of terahertz radiation," *Opt. Lett.*, vol. 32, no. 20, pp. 2945–2947, Oct. 2007.

[16] C. Themistos, B. M. A. Rahman, M. Rajarajan, K. T. V. Grattan, B. Bowden, and J. A. Harrington, "Characterization of Silver/Polystyrene (PS)-coated hollow glass waveguides at THz frequency," *J. Lightw. Technol.*, vol. 25, no. 9, pp. 2456–2462, Sep. 2007.

[17] L. J. Chen, H. W. Chen, T. F. Kao, J. Y. Lu, and C. K. Sun, "Low-loss subwavelength plastic fiber for terahertz waveguiding," *Opt. Lett.*, vol. 31, no. 3, pp. 308–310, Feb. 2006.

[18] C. S. Ponseca, Jr., R. Pobre, E. Estacio, N. Sarukura, A. Argyros, M. C. Large, and M. A. van Eijkelenborg, "Transmission of terahertz radiation using a microstructured polymer optical fiber," *Opt. Lett.*, vol. 33, no. 9, pp. 902–904, May 2008.

[19] M. Goto, A. Quema, H. Takahashi, S. Ono, and N. Sarukura, "Teflon photonic crystal fiber as terahertz waveguide," *Jpn. J. Appl. Phys.*, vol. 43, no. 2B, pt. 2, pp. L317–L319, Feb. 2004.

[20] H. Han, H. Park, M. Cho, and J. Kim, "Terahertz pulse propagation in a plastic photonic crystal fiber," *Appl. Phys. Lett.*, vol. 80, no. 15, pp. 2634–2636, Apr. 2002.

[21] K. Nielsen, H. K. Rasmussen, A. J. Adam, P. C. Planken, O. Bang, and P. U. Jepsen, "Bendable, low-loss topas fibers for the terahertz frequency range," *Opt. Exp.*, vol. 17, no. 10, pp. 8592–8601, May 2009.

[22] Y. S. Jin, G. J. Kim, and S. G. Jeon, "Terahertz dielectric properties of polymers," *J. Korean Phys. Soc.*, vol. 49, no. 2, pp. 513–517, Jan. 2006.

[23] G. Zhao, M. T. Mors, T. Wenckebach, and P. C. M. Planken, "Terahertz dielectric properties of polystyrene foam," *J. Opt. Soc. Amer. B, Opt. Phys.*, vol. 19, no. 6, pp. 1476–1479, Jun. 2002.

[24] J. Y. Lu, C. P. Yu, H. C. Chang, H. W. Chen, Y. T. Li, C. L. Pan, and C. K. Sun, "Terahertz air-core microstructure fiber," *Appl. Phys. Lett.*, vol. 92, no. 6, pp. 064105-1–064105-3, Feb. 2008.

[25] M. Skorobogatiy and A. Dupuis, "Ferroelectric all-polymer hollow Bragg fibers for terahertz guidance," *Appl. Phys. Lett.*, vol. 90, no. 11, pp. 113514-1–113514-3, Mar. 2007.

[26] K. Nielsen, H. K. Rasmussen, P. U. Jepsen, and O. Bang, "Porous-core honeycomb bandgap THz fiber," *Opt. Lett.*, vol. 36, no. 5, pp. 666–668, Mar. 2011.

[27] V. R. Almeida, Q. Xu, C. A. Barrios, and M. Lipson, "Guiding and confining light in void nanostructure," *Opt. Lett.*, vol. 29, no. 11, pp. 1209–1211, Jun. 2004.

[28] D. M. H. Leung, N. Kejalakshmy, B. M. A. Rahman, and K. T. V. Grattan, "Rigorous numerical analysis and characterization of a silicon vertical-slot nano-waveguide," *J. Nonlin. Opt. Phys. Mater.*, vol. 21, no. 1, pp. 125007-1–125007-18, Mar. 2012.

[29] M. Nagel, A. Marchewka, and H. Kurz, "Low-index discontinuity terahertz waveguides," *Opt. Exp.*, vol. 14, no. 21, pp. 9944–9954, Oct. 2006.
[30] N. Kejalakshmy, B. M. A. Rahman, A. Agrawal, H. M. Tanvir, and K. T. V. Grattan, "Metal-coated defect-core photonic crystal fiber for THz propagation," *J. Lightw. Technol.*, vol. 27, no. 11, pp. 1631–1637, Jun. 2009.
[31] P. J. St. Russell, "Photonic crystal fibers," *Science*, vol. 299, no. 5605, pp. 358–362, Jan. 2003.
[32] A. Hassani, A. Dupuis, and M. Skorobogatiy, "Porous polymer fibers for low-loss terahertz guiding," *Opt. Exp.*, vol. 16, no. 9, pp. 6340–6351, Apr. 2008.
[33] B. Ung, A. Mazhorova, A. Dupuis, M. Rozé, and M. Skorobogatiy, "Polymer microstructured optical fibers for terahertz wave guiding," *Opt. Exp.*, vol. 19, no. 26, pp. B848–B861, Dec. 2011.
[34] B. M. A. Rahman and J. B. Davies, "Finite-element analysis of optical and microwave waveguide problems," *IEEE Trans. Microw. Theory Tech*, vol. MTT-32, no. 1, pp. 20–28, Jan. 1984.
[35] J. P. Berenger, "Three-dimensional perfectly matched layer for the absorption of electromagnetic waves," *J. Comput. Phys.*, vol. 127, no. 2, pp. 363–379, Sep. 1996.
[36] K. Saitoh and M. Koshiba, "Numerical modeling of photonic crystal fibers," *J. Lightw. Technol.*, vol. 23, no. 11, pp. 3580–3590, Nov. 2005.
[37] M. Uthman, B. M. A. Rahman, N. Kejalakshmy, A. Agrawal, and K. T. V. Grattan, "Stabilized large mode area in tapered photonic crystal fiber for stable coupling," *IEEE Photon. J.*, vol. 4, no. 2, pp. 340–349, Apr. 2012.
[38] M. Heiblum and J. H. Harris, "Analysis of curved optical waveguides by conformal transformation," *IEEE J. Quantum Electron.*, vol. QE-11, no. 2, pp. 75–83, Feb. 1975.
[39] B. M. A. Rahman, M. Uthman, N. Kejalakshmy, A. Agrawal, and K. T. V. Grattan, "Design of bent photonic crystal fiber supporting a single polarization," *Appl. Opt.*, vol. 50, no. 35, pp. 6505–6511, Dec. 2011.
[40] B. M. A. Rahman, N. Kejalakshmy, M. Uthman, A. Agrawal, T. Wongcharoen, and K. T. V. Grattan, "Mode degeneration in bent photonic crystal fiber study by using the finite element method," *Appl. Opt.*, vol. 48, no. 31, pp. G131–G138, Nov. 2009.